Evaluation of q-Space Sampling Strategies for the Diffusion Magnetic Resonance Imaging

Haz-Edine Assemlal, David Tschumperlé, and Luc Brun

GREYC (CNRS UMR 6072), 6 Bd Maréchal Juin, 14050 Caen Cedex, France *

Abstract. We address the problem of efficient sampling of the diffusion space for the Diffusion Magnetic Resonance Imaging (dMRI) modality. While recent scanner improvements enable the acquisition of more and more detailed images, it is still unclear which q-space sampling strategy gives the best performance. We evaluate several q-space sampling distributions by an approach based on the approximation of the MR signal by a series expansion of Spherical Harmonics and Laguerre-Gaussian functions. With the help of synthetic experiments, we identify a subset of sampling distributions which leads to the best reconstructed data.

1 Introduction

The random Brownian motion of the water molecules is constrained by the microstructure of the brain white matter. The Diffusion Magnetic Resonance Imaging (dMRI) modality captures this local average displacement in each voxel using the pulse gradient spin echo sequence [1] and thus indirectly leads to images of the brain architecture. These images provide useful information to diagnose early stages of stroke and other brain diseases [2]. However, this average molecular displacement is not directly measured. Indeed, as the diffusion gradient pulse duration δ is negligible compared to the diffusion time Δ, the normalized MR signal E defined in the q-space is related to the average displacement Probability Density Function (PDF) P by the *Fourier transform* [3]

$$P(\mathbf{p}) = \int_{\mathbf{q}\in\mathbb{R}^3} E(\mathbf{q}) \exp(-2\pi i \mathbf{q}^{\mathrm{T}}\mathbf{p}) d\mathbf{q}, \quad \text{with } E(\mathbf{q}) = \frac{S(\mathbf{q})}{S_0}, \tag{1}$$

where $\mathbf{p}$ is the displacement vector and $\mathbf{q}$ stands for the diffusion wave-vector of the q-space. The symbols $S(\mathbf{q})$ and S_0 respectively denote the diffusion signal at gradient $\mathbf{q}$ and the baseline image at $\mathbf{q} = 0$.

Eq.(1) naturally suggests one should sample the whole q-space and use the Fourier transform to numerically estimate the PDF. This technique, known as Diffusion Spectrum Imaging (DSI) [4], is not clinically feasible mainly because of the long acquisition duration required to retrieve the whole set of needed q-space coefficients. As a result of DSI constraints, High Angular Resolution Diffusion Imaging (HARDI) [5] has come as an interesting alternative and proposes to

* We are thankful to Cyceron for providing data and the fruitful technical discussions.

sample the signal on a single sphere of the q-space. Most of the methods of the literature working on HARDI images [6–9] consider a single shell acquisition and have thus to assume strong priors on the radial behavior of the signal, classically a *mono*-exponential decay for instance.

Sampling schemes on several spheres in the q-space have been only proposed very recently [9–14]. Since the number of samples still remains too low for computing the Fourier transform, proposed methods rather consider computed tomography technique [13] or approximations of the MR signal radial attenuation by multi-exponential functions [9, 11]. Note that even if these methods use a larger set of data, they are still using *a-priori* models of the radial behavior of the input signal. In section 2, we first overview the mathematical background of one previous diffusion features estimation method introduced in [15, 16]. Then, we review several q-space sampling strategies proposed so far in the literature and detail the evaluation procedure of the experiments in section 3. We conclude on the results in section 4.

2 Spherical Polar Fourier Expansion

To be as self-contained as possible, we briefly overview our previous estimation method introduced in [15, 16] based on the Spherical Polar Fourier (SPF) expansions. In order to be able to reconstruct the PDF from Eq.(1) even with few samples, we seek to build a basis in which the acquired signal is sparse.

Let E be the normalized MR signal attenuation. We propose to express it as a series in a spherical orthonormal basis named Spherical Polar Fourier (SPF) [17]:

$$E(\mathbf{q}) = \frac{S(\mathbf{q})}{S(0)} = \sum_{n=0}^{\infty} \sum_{l=0}^{\infty} \sum_{m=-l}^{l} a_{nlm} R_n(||\mathbf{q}||) y_l^m \left(\frac{\mathbf{q}}{||\mathbf{q}||} \right), \tag{2}$$

where a_{nlm} are the expansion coefficients, y_l^m are the real Spherical Harmonics functions (SH), and R_n is an orthonormal radial basis function.

The angular part of the signal E then is classically reconstructed by the complex SH Y_l^m which form an orthonormal basis for functions defined on the single sphere. They have been widely used in diffusion MRI [18]. Indeed, as the diffusion signal exhibits real and symmetric properties, the use of a subset of this complex basis restrained to real and symmetric SH y_l^m strenghten the robustness of the estimated reconstruction to signal noise and reduces the number of required coefficients [18].

Meanwhile, the radial part of the signal E is reconstructed in our approach [15, 16] by the elementary radial functions R_n. A sparse representation of the radial signal should approximate it in a few radial order N. Based on these observations, we propose to estimate the radial part of E using the normalized generalized Gaussian-Laguerre polynomials R_n:

$$R_n\left(||\mathbf{q}||\right) = \left[\frac{2}{\gamma^{3/2}} \frac{n!}{\Gamma\left(n + 3/2\right)} \right]^{1/2} \exp\left(-\frac{||\mathbf{q}||^2}{2\gamma} \right) L_n^{1/2}\left(\frac{||\mathbf{q}||^2}{\gamma} \right), \tag{3}$$

where γ denotes the scale factor and $L_n^{(\alpha)}$ are the generalized Laguerre polynomials. The Gaussian decay arises from the normalization of the Laguerre polynomials in spherical coordinates.

The SPF forms an orthonormal basis where a low order truncation assumes a radial Gaussian behavior as in [9, 11] and a high order truncation provides model-free estimations. Besides, the square error between a function and its expansion in SPF to order $n <= N$ and $l <= L$ converges to zero as N and L go to infinity. We fit the signal to the SPF by a damped least square minimization procedure. The best fitting coefficients a_{nlm} are thus given by a regularized Moore-Penrose pseudo-inverse scheme:

$$\mathbf{A} = \arg\min_{\mathbf{A}} ||\mathbf{E} - \mathbf{M}\mathbf{A}||^2 + \lambda_l ||\mathbf{L}||^2 + \lambda_n ||\mathbf{N}||^2 = (\mathbf{M}_{reg})^{-1}\mathbf{M}^{\mathrm{T}}\mathbf{E} \qquad (4)$$

where $\mathbf{M} = (R_n(||\mathbf{q}_j||)y_l^m(\frac{\mathbf{q}_j}{||\mathbf{q}_j||}))_{nlm\times j\in\mathbb{N}^3\times\mathbb{N}}$ denotes the SPF basis matrix, $\mathbf{M}_{reg} = \mathbf{M}^{\mathrm{T}}\mathbf{M} + \lambda_n\mathbf{N}^{\mathrm{T}}\mathbf{N} + \lambda_l\mathbf{L}^{\mathrm{T}}\mathbf{L}$ and $\mathbf{E}, \mathbf{A}$ respectively denote the vectors $(E(\mathbf{q}_1), \ldots, E(\mathbf{q}_{ns}))^{\mathrm{T}}$ and $(a_{000}, \ldots, a_{NLL})^{\mathrm{T}}$. Since the matrix $\mathbf{M}_{reg}$ is likely to be ill-conditioned because of the highly reduced number of samples, we use regularization matrices $\mathbf{L}$ and $\mathbf{N}$ with entries $l^2(l+1)^2$ and $n^2(n+1)$ along their diagonal. They penalizes high variations of the angular and radial parts of SPF in the estimation under the assumption that they are likely to capture signal noise. The symbols λ_l and λ_n respectively denote angular and radial regularization weights.

3 Material and Methods

The number of data samples is limited because of the restricted acquisition. So the sampling scheme is actually something critical and should be chosen wisely. Indeed, given a fixed number of samples (clinical constraint), which repartition of the q-space samples is the best ? Which radial order truncation N should be chosen to fit Gaussian or bi-Gaussian MR datasets ? All these questions about the acquisition protocol are the focus of the following experiments.

3.1 *q*-space sampling

Let $n_s \in \mathbb{N}$ be the total number of samples and $n_b \in \mathbb{N}$ the number of sampling sphere. Let f be the number of samples on one sphere $x \in [1, n_b]$ so that

$$f_x(\eta) = \frac{q_x^\eta}{\sum_{i=1}^{n_b} q_i^\eta} n_s, \quad \text{and} \quad q_i(\beta) = \left(\frac{i-1}{n_b - 1}\right)^\beta (q_{max} - q_{min}) + q_{min} \qquad (5)$$

where $q_i \in [q_{min}, q_{max}]$ refers to the radius of the i-th sphere. For simplicity sakes, the radii are considered as uniformly distributed ($\beta = 1$) between $[q_{min}, q_{max}] = [1, 30]\,\mathrm{cm}^{-1}$. The sampling points on each sphere should be as evenly spread as possible and are thus computed by electrostatic energy minimization as proposed in [14]. The spheres which possess very few samples are

Table 1: Overview of the different considered strategies for the q-space sampling. From a fixed number of total samples $n_s = 300$ and spheres n_b, the parameter η sets the spherical repartition of samples in the q-space as described by Eq.(5). The radii of the spheres are uniformly distributed ($\beta = 1$).

	$\eta = -2$	$\eta = -1$	$\eta = 0$	$\eta = 1$	$\eta = 2$	$\eta = 3$
$n_b = 2$	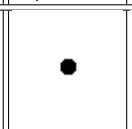					
$n_b = 5$	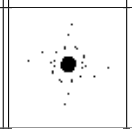					
$n_b = 10$	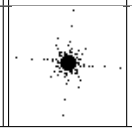					

randomly rotated to capture more signal ($f_x(\eta) \leq 6$ in our experiments). Overall, $f(\eta = 0)$ corresponds to a constant number of samples on each sphere as described in [13, 15, 19]. $f(\eta = 2)$ corresponds to a uniform spherical sampling as introduced in [11, 12].

3.2 Data processing

The following multi-exponential model was used to generate the considered synthetic data,

$$E(\mathbf{q}) = E(q \cdot \mathbf{u}) = \sum_{k=1}^{N_f} f_k \exp\left(-\frac{(q - m_k)^2 \mathbf{u}^{\mathrm{T}} \mathbf{D}_k \mathbf{u}}{2\,\sigma^2}\right) \tag{6}$$

where $\sum_{k=1}^{N_f} f_k = 1$ and $||\mathbf{u}|| = 1$. The symbol N_f stands for the number of fibers, m_k is the mean diffusion and $\mathbf{D}_k$ is a 3×3 symmetric definite positive matrix defining the diffusion anisotropy for the k-th fiber. The scale factor γ was calculated on the data samples using the Apparent Diffusion Coefficient (ADC) with a linear least square fit so that $\gamma = (2\,\mathrm{ADC})^{-1}$. Thus the decay of the SPF basis eigenfunctions at order $n = 0$ have the same scale as the sampled data. For a single fiber configuration as in Fig.1b, $\mathrm{diag}(\mathbf{D}_k) = [1.5; 0.2; 0.2]\,\mathrm{mm^2 s^{-1}}$ and $\sigma = 5$.

In Fig.2, we determine which truncation order is sufficient to capture the standard data pattern presented in Fig.1. The normalized error of the power spectrum between the original and reconstructed data is expressed as

$$\text{Normalized Error} = \frac{\sum_{i=1}^{n_s} E[\mathbf{q}_i]^2 - \sum_{n=0}^{N} \sum_{l=0}^{L} \sum_{m=-l}^{l} a_{n,l,m}^2}{\sum_{i=1}^{n_s} E[\mathbf{q}_i]^2} \tag{7}$$

(a) Isotropic (b) One fiber (c) Crossing fibers (d) Bi-Gaussian

Fig. 1: Some standard pattern of q-space local diffusion data in the human brain white matter. Data are centered on a volumic image of size $64 \times 64 \times 64$.

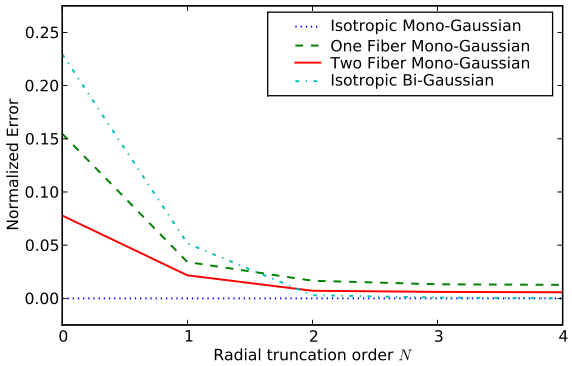

Fig. 2: Influence of radial truncation order N on the normalized error between the power spectrum of the original data and its reconstruction in the proposed basis. The number of samples is $n_s = 64^3$. The angular truncation order is $L = 4$.

The condition number C is an interesting index as it relates the correspondence between the sampling distribution and the reconstruction basis, *independently of the data*. It measures how numerically well-conditioned the regularized matrix $\mathbf{M}_{reg}$ from Eq.(4) is,

$$C = ||\mathbf{M}_{reg}||_\infty ||\mathbf{M}_{reg}^{-1}||_\infty \tag{8}$$

Fig.3 shows a comparison between several sampling strategies, which were generated according to Eq.(5). This figure illustrates the evolution of the reconstruction quality along with the number of sampling spheres n_b and the repartition of samples η on each sphere. Only the crossing fibers data configuration is illustrated in this experience as we found no significant differences with other data configuration. Fig.4 illustrates for the same experiment qualitative results for good and bad reconstruction. Fig.5 shows the comparison of two sampling schemes: non-uniform and uniform sampling of the q-space, respectively $\eta = 0$ and $\eta = 2$. The case $f(\eta = 2)$ corresponds to a uniform sampling considering spherical coordinates. $n_s = 300$, $n_b \in [1, 10]$ and the angular truncation order is set to $L = 4$.

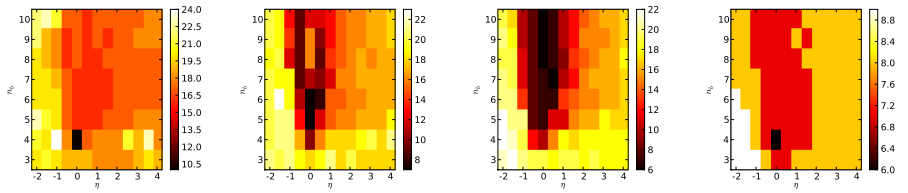

(a) n_s=120 No regularization. (b) n_s = 200 No regularization. (c) n_s = 300 No regularization. (d) n_s=120. With regularization.

Fig. 3: Condition number C evolution with the sampling distribution η and the number of sampling sphere n_b. The lower C is, the more stable the reconstruction is. The symbol n_s denotes the total number of samples. Angular truncation order is $L = 4$. Radial truncation order is $N = 3$, consequently $n_b \geq 3$ (120 coefficients). (d) Radial and angular regularization weights: $\lambda_n = 10^{-4}$, $\lambda_l = 10^{-6}$. Data simulates crossing fibers diffusion signal Fig.1c.

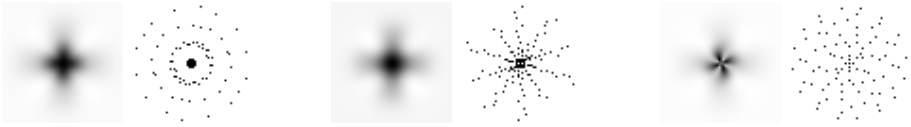

(a) PSNR=40.23 dB (b) PSNR=39.98 dB (c) PSNR=27.54 dB

Fig. 4: Example of some sampling distributions and their respective reconstruction.

4 Results and Discussion

Fig.2 illustrates that a reasonably good radial truncation order N depends on the MR data pattern (*c.f.* Fig.1). Nonetheless, in all our experiments with standard data configurations in the brain white matter, the convergence to the data truth is achieved with N = 3. Concerning the sampling distribution η, the results of Fig.3 indicate that the best sampling distribution is $\eta \in [-1, 2]$, especially in the case of a small number of total samples (*c.f.* Fig.3(a-c)). This result is in accordance with the propositions already found in literature [11, 12, 15, 19]. Therefore, Fig.5 shows a deeper comparison of two sampling $\eta = 0$ and $\eta = 2$. Fig.5(a) shows the evolution of C the condition number along with the number of sampling sphere n_b and the radial truncation order N. As expected, C is very high when $N > n_b$ and leads to very unstable results. When $N \leq n_b$, the condition number increases slowly along with increasing values of N and is quite constant along variations of n_b. Results obtained using the non-uniform sampling exhibit more monotonous evolutions than with the uniform sampling.

Fig.5(b) and (c) illustrate the PSNR (Peak Signal to Noise Ratio) evolution of the reconstruction of a Gaussian mixture MR signal. Although the maximum of the PSNR for all sampling protocols are quite the same (≈ 40) (*c.f.* Fig.3), it is clear that the non-uniform sampling protocol ($\eta = 0$) is more robust to wrong values of N and n_b. Besides, the robustness to wrong values of the scale factor γ is illustrated by the lines of Fig.5b. Indeed, the first order $N = 0$ of the SPF basis has a Gaussian decay and should entirely capture an isotropic

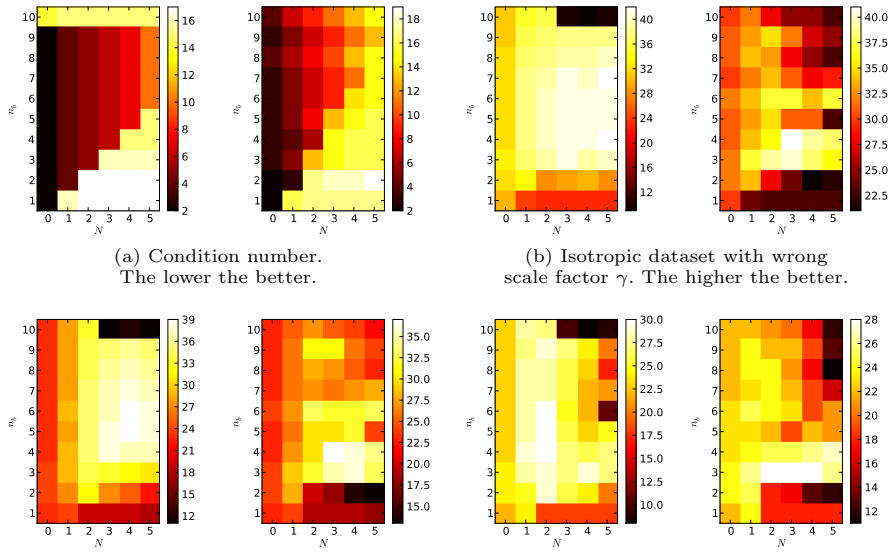

(a) Condition number. The lower the better.

(b) Isotropic dataset with wrong scale factor γ. The higher the better.

(c) Bi-Gaussian dataset. The higher the better.

(d) Bi-Gaussian noisy dataset. The higher the better.

Fig. 5: Comparison of uniform ($\eta = 2$) vs non-uniform ($\eta = 0$) sampling (respectively left and right image) on Gaussian and bi-Gaussian isotropic datasets. N stands for the radial truncation in the SPF basis and n_b is the number of sampling sphere in the q-space. (b) Isotropic data with $\sigma^2 = 25$ (Fig.1a), with erroneous scale factor $\gamma = 5\sigma^2$. (d) The input data are noised with Rician noise (PSNR=18.9 dB).

Gaussian data (*c.f.* Fig.2). In Fig.5b, we set an arbitrary erroneous scale factor value γ not adapted to the signal decay σ so that $\gamma/\sigma^2 = 5$. The signal is reconstructed for $N \geq 3$ in accordance to Fig.2. Once again, Fig.5b shows that the non-uniform sampling protocol is the most robust to wrong values of γ. Finally, Fig.5d shows the results on a bi-Gaussian noisy dataset, estimated using our damped linear least square method Eq.(4). Besides the lower PSNR average compared to Fig.5c, it is remarkable that best results of Fig.5d were also obtained from lower radial truncation order N than Fig.5c. Indeed, a reconstruction using high N can significantly capture more noise than using lower N.

Out of the results, the non-uniform sampling protocol ($\eta = 0$) gives better global results than the uniform protocol ($\eta = 2$). The best reconstructions are obtained for $N \approx 3$ and $n_b \approx 4$. It confirms that a better reconstruction of the low q-space frequencies of the MR signal leads to a better reconstruction of the whole signal since low frequencies really carry the greatest part of the MR signal. Note that in contrast to our conclusion, Jones *et al.* in [14] interestingly observed in the restricted case of DTI with 2 spheres that more samples in the outer sphere gives the best results. This result might be explained by the strong restrictions of DTI to capture a Gaussian signal. Nonetheless, it is important to stress that the optimal parameters in this work are for the SPF basis.

5 Conclusion

In this paper, we proposed a unifying diffusion estimation formalism able to study the effect of several sampling schemes already proposed in the literature. We evaluated the influence of these schemes on the quality of the reconstruction for different shapes of diffusion signal. Out of the results, our findings indicate it is preferable to favour a high density of samples with low diffusion gradients rather than high diffusion gradients. We successfully identified a subset of sampling schemes which gives the best performances in adequacy with realistic clinical constraints.

References

1. Stejskal, E., Tanner, J.: Spin diffusion measurements: spin echoes in the presence of a time-dependent field gradient. Journal of Chemical Physics **42** (1965) 288–292
2. LeBihan, D., Breton, E., Lallemand, D., *et al.*: Mr imaging of intravoxel incoherent motions: Application to diffusion and perfusion in neurologic disorders. Radiology (1986) 401–407
3. Callaghan, P.: Principles of Nuclear Magnetic Resonance Microscopy. Oxford University Press, USA (1991)
4. Wedeen, V., Reese, T., Tuch, D., *et al.*: Mapping fiber orientation spectra in cerebral white matter with fourier transform diffusion mri, ISMRM (2000) 82
5. Tuch, D., Weisskoff, R., Belliveau, J., Wedeen, V.: High angular resolution diffusion imaging of the human brain. (1999) 321
6. Tuch, D.: Q-ball imaging. Magn Reson Med **52** (2004) 1358–1372
7. Yablonskiy, D.A., Bretthorst, G.L., Ackerman, J.J.: Statistical model for diffusion attenuated mr signal. Magn Reson Med **50** (2003) 664–669
8. Liu, C., Bammer, R., Acar, B., Moseley, M.: Characterizing non-gaussian diffusion by using generalized diffusion tensors. Magn Reson Med **51** (2004) 924–937
9. Özarslan, E., Sherperd, T.M., Vemuri, B.C., *et al.*: Resolution of complex tissue microarchitecture using the diffusion orientation transform (dot). NeuroImage **31** (2006) 1086–1103
10. Cercignani, M., Alexander, D.: Optimal acquisition schemes for in vivo quantitative magnetization transfer mri. Magn. Reson. Med. **56** (2006) 803–810
11. Assaf, Y., Basser, P.J.: Composite hindered and restricted model of diffusion (charmed) mr imaging of the human brain. NeuroImage **27** (2005) 48–58
12. Wu, Y.C., Alexander, A.L.: Hybrid diffusion imaging. NeuroImage **36** (2007)
13. Pickalov, V., Basser, P.J.: 3d tomographic reconstruction of the average propagator from mri data, ISBI (2006)
14. D.K. Jones, M.A. Horsfield, A.S.: Optimal strategies for measuring diffusion in anisotropic systems by magnetic resonance imaging. Magnetic Resonance in Medicine **42**(3) (1999) 515–525
15. Assemlal, H.E., Tschumperlé, D., Brun, L.: Efficient computation of pdf-based characteristics from diffusion mr signal, MICCAI (2008) 70–78
16. Assemlal, H.E., Tschumperlé, D., Brun, L.: Robust variational estimation of pdf functions from diffusion mr signal, CDMRI, MICCAI Workshop (2008)
17. Ritchie, D.W.: High-order analytic translation matrix elements for real-space six-dimensional polar fourier correlations. J. Appl. Cryst. **38** (2005) 808–818
18. Frank, L.: Characterization of anisotropy in high angular resolution diffusion-weighted mri. Magn Reson Med **47** (2002) 1083–1099
19. Khachaturian, M., Wisco, J., Tuch, D.: Boosting the sampling efficiency of q-ball imaging using multiple wavevector fusion. Magn Reson Med **57** (2007) 289–296